

Ilias Bosdas

Laboratory for Energy Conversion,
Department of Mechanical and
Process Engineering,
ETH Zurich,
Zurich 8092, Switzerland
e-mail: bosdas@lec.mavt.ethz.ch

Michel Mansour

Laboratory for Energy Conversion,
Department of Mechanical and
Process Engineering,
ETH Zurich,
Zurich 8092, Switzerland
e-mail: michel.mansour@lec.mavt.ethz.ch

Anestis I. Kalfas

Department of Mechanical Engineering,
Aristotle University of Thessaloniki,
Thessaloniki 54124, Greece
e-mail: akalfas@auth.gr

Reza S. Abhari

Laboratory for Energy Conversion,
Department of Mechanical and
Process Engineering,
ETH Zurich,
Zurich 8092, Switzerland
e-mail: rabhari@lec.mavt.ethz.ch

Shigeki Senoo

Mitsubishi Hitachi Power Systems, Ltd.,
3-1-1, Saiwai,
Hitachi 317-0073, Ibaraki, Japan
e-mail: shigeki1_senoo@mhps.com

Unsteady Flow Field and Coarse Droplet Measurements in the Last Stage of a Low-Pressure Steam Turbine With Supersonic Airfoils Near the Blade Tip

The largest share of electricity production worldwide belongs to steam turbines. However, the increase of renewable energy production has led steam turbines to operate under part load conditions and increase in size. As a consequence, long rotor blades will generate a relative supersonic flow field at the inlet of the last rotor. This paper presents a unique experiment work that focuses at the top 30% of stator exit in the last stage of a low pressure (LP) steam turbine test facility with coarse droplets and high wetness mass fraction under different operating conditions. The measurements were performed with two novel fast response probes: a fast response probe for three-dimensional flow field wet steam measurements and an optical backscatter probe for coarse water droplet measurements ranging from 30 μm up to 110 μm in diameter. This study has shown that the attached bow shock at the rotor leading edge is the main source of interblade row interactions between the stator and rotor of the last stage. In addition, the measurements showed that coarse droplets are present in the entire stator pitch with larger droplets located at the vicinity of the stator's suction side. Unsteady droplet measurements showed that the coarse water droplets are modulated with the downstream rotor blade-passing period. This set of time-resolved data will be used for in-house computational fluid dynamics (CFD) code development and validation.

[DOI: 10.1115/1.4036011]

Introduction

Steam turbines are widely used in power generation and provide the world with more than 60% of its entire generated electrical power. In order to stay competitive in the face of the growing renewable energy market, steam turbines require operational flexibility. Operational flexibility indicates that part load conditions have increased in time on the overall operating period of the machine. In addition, the continuous increase in energy demand necessitates efficient design of the steam turbines as well as power output augmentation. This implies that the area of the last stages is continuously being increased, leading to blade lengths of up to 60 in. [1,2]. This poses a design challenge as relative supersonic flow speeds [3,4] at the blade tip region are present under different wetness mass fractions and droplets sizes that range from few micrometers up to 100 μm in diameter [5]. The aerodynamic design of the last stage of the low-pressure steam turbine has a direct impact on its mechanical robustness as the unsteady flow field is highly correlated with the mechanical vibrations and the high relative droplet velocities with erosion phenomena on the tip region of the last rotor. Regarding the power output, the contribution of the last stage is in the range of 20% which shows the significance for an efficient design [4].

The relative supersonic speed at the inlet of the last rotor generates a shock wave at the rotor's leading edge which results in elevated unsteady stator rotor interactions, as described by Senoo

and Ono [6]. Consequently, there is a need for time-resolved measurements; however, the severe environment in wet steam at the last stages only allowed for a few attempts of unsteady pressure measurements [2,7,8]. According to the authors' knowledge, time-resolved measurements in the wet steam environment with supersonic relative flows at the rotor inlet have never been reported in the open literature. In addition, advanced CFD models capable of solving two-phase three-dimensional flows require experimental data for validation [9], and therefore the need for time-resolved measurements becomes unavoidable.

Droplet measurements are very challenging due to the very small sizes of water particles at the last stage of LP steam turbines (0.1–200 μm). The measurement of droplet size distribution in two-phase flows is of high interest due to high erosion rate of the blades at the rotor leading edge and trailing edge of the last stage reducing their aerodynamic efficiency and expected lifetime [5]. There are a significant number of publications that have developed different probe types for measuring the size and concentration of water droplets [10]. Some of the first attempts were made by Walters and Skingley [11,12] and Tatsuno and Nagao [13] with light extinction probes for fog droplet measurements. The light extinction technique is also used in Ref. [14] for particle measurements in steam turbines with significant results in fog droplet diameters and wetness mass fractions. It is worth mentioning the work of Young and Yeoh in Ref. [15], which presents measurements of fog and coarse water droplets for the first time at the inlet and exit of the last stage. In their report, Young et al. provide single traverse time-averaged measurements with water flows (droplets and casing film flows) as well as the total flow rates of coarse water droplets entering and exiting the last stage.

Contributed by the Controls, Diagnostics and Instrumentation Committee of ASME for publication in the JOURNAL OF ENGINEERING FOR GAS TURBINES AND POWER. Manuscript received July 26, 2016; final manuscript received February 15, 2017; published online April 11, 2017. Editor: David Wisler.

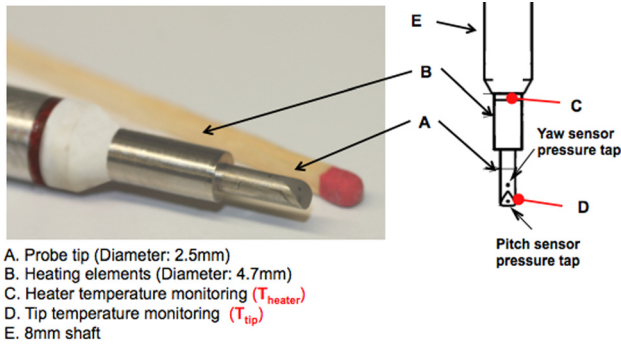


Fig. 1 FRAP-HT heated probe schematic and temperature measurement locations

A number of recent developments have led to a combination of optical and pneumatic probes within one system for droplet measurements in steam turbines. These probes combine a pneumatic part of time-averaged pressure measurements and an optical part of wetness fraction measurements in the last stages of the machine [14,16]. Cai et al. [17] have developed an integrated probe system for coarse water droplet measurements up to $400\ \mu\text{m}$. The probe consists of a fog droplet measurement subsystem using light extinction technique and a coarse droplet measurement subsystem using the forward light scattering technique. The tip diameter is 20 mm, and it incorporates as well a pneumatic part for time-averaged flow field measurements. In their results, they correlate the erosion location at the rotor leading edge with the droplets' diameter and trajectories. The work of Fan et al. [18] on probe development for coarse droplet measurements with imaging technique is noteworthy. In their report, they present a video-probe system capable of taking images of coarse water droplets ($D_d > 10\ \mu\text{m}$) in order to measure their diameter and velocity. The main drawbacks of the last two approaches are the relatively large size of the probe tips ($D_p > 20\ \text{mm}$) and the low measurement bandwidth, which constrains the measurements to a time-averaged flow field analysis.

This paper presents a unique set of time-resolved flowfield and coarse water droplet measurements conducted at the stator exit of the last stage of MHPS's LP steam turbine test facility in Japan. The measurements were performed with a novel fast response heated probe (FRAP-HTH) for time-resolved steam flowfield measurements [19] and with an optical backscatter probe (FRAP-OB) for coarse droplet measurements ($D_d > 30\ \mu\text{m}$) [20]. In the current measurement campaign, a circumferential traversing system enabled plane measurements covering more than one stator pitch at the nozzle exit of L-0 stage in MHPS steam turbine

facility. The FRAP-HTH and FRAP-OB measurements enabled the identification of unsteady flow field features and coarse droplet formation mechanisms responsible for the overall performance of large LP steam turbines. Further results from measurements conducted in MHPS facility in previous campaigns with the FRAP-HTH probe can be found in Refs. [19] and [21].

Fast Response Instrumentation for Wet Steam Conditions

Two novel miniature probes have been used extensively in the current experimental work: the FRAP-HTH probe for unsteady wet steam flow field measurements and the FRAP-OB probe for coarse water droplet measurements. The FRAP-HTH and FRAP-OB probes are shown in Figs. 1 and 2, respectively. Figure 2 shows a schematic with the operating principle of the FRAP-OB, which is based on the backscatter light when a water droplet crosses the sample volume of the probe.

FRAP-HTH Operating Principle. As presented in Refs. [19] and [22], the FRAP-HTH probe is an improved version of the FRAP-HT probe developed in the LEC at ETH Zurich. The probe consists of two pressure taps one for yaw angle sensitivity (yaw pressure tap) and one for pitch angle sensitivity (pitch sensor pressure tap). It has a tip diameter of 2.5 mm and a length of 1.3 m. The measurement bandwidth of the FRAP-HTH probe due to the resonant cavity effect of the pressure taps has been measured in air at 21 kHz, which sets the eigenfrequency to 25.3 kHz for the current steam condition. In order to operate the probe with unlogged pressure taps, the probe tip is heated to a few degrees above the flow saturation temperature via a miniature high power density heater. The robust design of the FRAP-HTH consists of shielded pressure taps for protecting the miniature fast pressure sensors from direct water droplet impacts. As shown in Fig. 1, the probe tip (A) is heated using a miniature heater (B) located close to the probe tip. The temperature of the heater and the pressure sensors are monitored continuously, and the probe tip temperature is controlled using a closed-loop (proportional–integral–derivative) PID controller. In order to ensure the highest absolute measurement accuracy, the probe tip is kept at a constant temperature at each measurement point of the overall measurement grid.

The probe is calibrated for a given range of probe relative yaw and pitch angles as well as at different Mach numbers in the Free-jet calibration facility of the Laboratory for Energy Conversion at ETH Zurich. Two sets of calibration coefficients are defined depending on the main flow field direction, and as a result the model of aerodynamic calibration coefficients is divided into two sectors. This choice is made according to measurement of the two piezoresistive sensors P_{yaw} and P_{pitch} . As presented in Ref. [19],

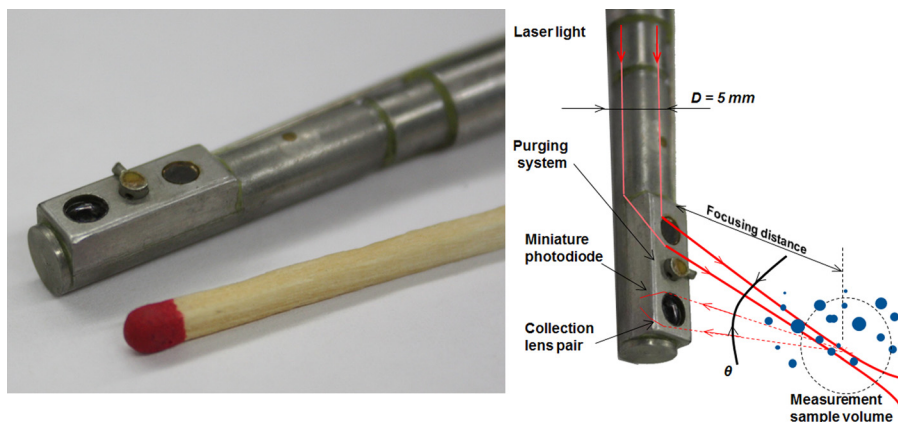


Fig. 2 FRAP-OB probe tip with purging interface for windows protection from water contamination and beam deflection

Table 1 FRAP-HTH uncertainty calculation for the nozzle exit of the last stage of the LP steam turbine

Parameter:	Expanded abs. Uncertainty	
	Sector 1	Sector 2
φ	± 0.30 deg	± 0.20 deg
Γ	± 0.49 deg	± 0.10 deg
P_t	± 210 Pa (1.0%Pt)	± 170 Pa (0.6%Pt)
P_s	± 480 Pa (2.3%Ps)	± 390 Pa (1.9%Ps)
Ma	± 0.03	± 0.02
Ma _{rel}	± 0.02	± 0.017
C _{pt}	$\pm 0.6 \times 10^{-3}$	$\pm 0.5 \times 10^{-3}$
C _{ps}	$\pm 1.5 \times 10^{-3}$	$\pm 1.2 \times 10^{-3}$

Table 2 Operating tested condition

	OP-1	OP-2	OP-3
Massflow (ton/h)	47.5	35	35
Exit pressure (kPa)	5.0	5.0	5.0
Inlet temperature (°C)	272	272	220
Calculated wetness mass fraction at L-0 stator exit at 80% span (%)	4.0	3.6	6.2

the first set of aerodynamic calibration coefficients is used when the $P_{yaw} > P_{pitch}$, which implies low flow pitch angles. The second set of aerodynamic coefficients is used for high pitch flow angles when the pressure signal from the pitch sensor (P_{pitch}) is greater than the pressure signal from the yaw sensor (P_{yaw}). For the current measurement campaign, the probe was calibrated with an extended pitch angle range of $-5 \text{ deg} < \text{pitch} < 49 \text{ deg}$ and for a yaw angle range of $-26 \text{ deg} < \text{yaw} < +26 \text{ deg}$ as presented in Refs. [19] and [22] due to the high flair angle of the low-pressure stage of the steam turbine.

The uncertainty calculation of the FRAP-HTH probe was performed using the Guide to the Expression of Uncertainty in Measurement (GUM). This is commercial software where the whole chain of uncertainty sources was imported and calculated accordingly. The overall uncertainties for the two sectors as described in the previous paragraph for the operating condition OP-1 (see Table 2) measured at the nozzle exit of the last stage of the test facility are presented in Table 1. In general, sector 1 exhibits greater values of uncertainties in all flow parameters. The main reason is the higher error arising from the aerodynamic calibration model fit. The maximum total and static pressure uncertainties are 1% and 2.3% of the total and static pressures, respectively. This enables accurate measurements in the challenging wet steam environment of the machine. The total and static pressure coefficients are defined in Eqs. (1) and (2), respectively. The inlet refers to the conditions at the inlet of the machine, and the exit refers to the conditions at the exit of the machine (see Fig. 4)

$$C_{pt} = \frac{P_{t,FRAP-HTH} - P_{s,exit}}{P_{t,inlet} - P_{s,exit}} \quad (1)$$

$$C_{ps} = \frac{P_{s,FRAP-HTH} - P_{s,exit}}{P_{t,inlet} - P_{s,exit}} \quad (2)$$

FRAP-OB Operating Principle. For the coarse droplet measurements, the miniature FRAP-OB probe (Fig. 2) was used. The probe design and operating principle are described in detail in Ref. [20]. This instrument is an optical backscatter probe, which has an embedded fast response miniature photodiode with a bandwidth of 30 MHz and enables time resolve droplet measurements with droplet speeds of up to 170 m/s. The probe has a tip diameter

of 5.5 mm and an overall length of 1.3 m to access the flow path of the last LP steam turbine stage. The measurement range for the droplet diameters of the FRAP-OB is from 30 to 110 μm .

Light is guided inside the probe tip through an optical fiber and is then focused three probe diameters far from the tip forming a measurement sample volume. For this purpose, a monochromatic ($\lambda = 632 \text{ nm}$) He-Ne laser is used. As indicated in Fig. 2, when droplets cross the focused sample volume, they scatter light in all directions. However, a set of collecting lenses captures the backscatter light, which is then focused in the miniature photodiode. As a result, each droplet that crosses the sample volume of the FRAP-OB probe is recorded. The reduction of the incidence and backscatter light intensity due to light extinction would result in a proportional decrease of the probe's amplitude response curve. The error of the probe in measured droplet diameter is calculated below 5% (see Table 2), for the worse case of 6.2% wetness, assuming a Sauter mean droplet diameter of 10 μm and a fog droplet concentration of 10^{10} droplets/ m^3 . The probe tip is equipped as well with an active purging system in order to keep the windows clean from any water contamination and laser beam deflection. The purging flow is attached to the surface of the windows in order to minimize any interaction with the surrounding flow field.

The FRAP-OB probe is calibrated with a monodispersed droplet generator developed by Rollinger et al. [23]. The device is capable of producing monodispersed water droplets with an accuracy of $\pm 2 \mu\text{m}$ in diameter. Water droplets are generated continuously with a frequency and air-backpressure set by the user. Depending on the tuning parameters, the droplets' velocity ranges from 4 to 12 m/s. For independent reference measurements of the droplet diameter, a high-resolution camera is utilized. A strobe light illuminates the generated water droplets, and the shadow imaging technique is used to take pictures of them. In a second step, the pictures are processed, and the droplets' diameter is calculated. At the maximum amplification factor, there is an error range of $\pm 0.69 \mu\text{m}$ in droplet diameter. In the last step of the calibration process, the probe's output voltage signal is correlated with the measured droplets' diameter from the pictures, and the calibration curve of the FRAP-OB is derived by applying an exponential model curve fit. As presented in Ref. [20], the maximum uncertainty of the probe for the droplet diameter, calculated with the GUM workbench, is $\pm 5.4 \mu\text{m}$.

In addition to size measurements, the FRAP-OB probe is calibrated for the droplets' speed. During the calibration procedure, the speed of the droplets is measured through the generated pictures by calculating the actual distance between two consequent droplets and multiplying the operating frequency of the device set by the frequency generator.

Experimental Facility

All measurements of the current work were conducted at MHPS' research steam turbine test facility in Hitachi, Ibaraki, Japan. The facility is described by Haraguchi et al. [1]. As shown in Fig. 3, it is a four-stage low-pressure steam turbine (L-3 to L-0) rig with a scale ratio of 1/3. The steam is generated in the boiler and directed into the turbine inlet. The inlet pressure and temperature are controlled in order to test different operating conditions and loads. At the exit of the last stage of the machine, the condenser controls the exit absolute static pressure, and the condensate water is guided back to the boiler to close the cycle. The facility also includes an inverter motor to drive the turbine shaft during low load tests. The inverter motor generator and a water brake dynamometer absorb the turbine's generated power and control the rotational speed of the machine through a gearbox. The newly developed last stage rotor blades are a downscaled model of actual 50 in. steam turbine blades, enabling supersonic relative flow speeds at the blade tip region. The measurements were performed at a rated speed of 10,800 rpm. The main



Fig. 3 MHPS' low-pressure steam turbine test facility where FRAP-HTH and FRAP-OB measurements were conducted

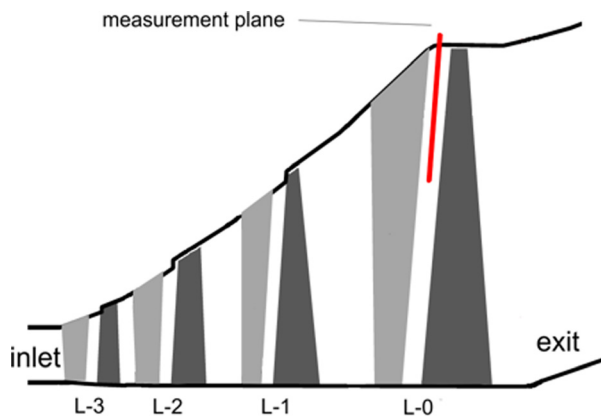


Fig. 4 Test section schematic of MHPS's steam turbine test facility. The measurement plane of the probe at L-0 stator exit is indicated as well.

operating tested conditions presented in the current paper are summarized in Table 2.

As shown in Fig. 4, all measurements of the current experimental work were conducted at the stator exit of the last stage (L-0).

There are 48 rotor and 58 stator blades. In addition, the stator blades were equipped with moisture separating slits (suction slits). This specific feature is installed at the outer range of the blade span. It is located on stator's pressure side, and its main goal is to remove the water film, which builds up on the blade surface and then periodically tears from the trailing edge. The data are acquired at a sampling rate of 200 kHz for the FRAP-HTH probe and 1 MHz for the FRAP-OB probe over time periods of 2 and 1 s, respectively. All measurements approximately cover the last 30% of the blade span for one stator pitch. The grid at the measurement plane consists of 21 radial traverses with each traverse including 19 points in the radial direction for OP-1 measured with the FRAP-HTH probe. The FRAP-HTH measurement plane is located at $x/s = 0.35$ between L-0 stator and rotor, and the FRAP-OB plane is located at $x/s = 0.02$.

Results and Discussion

Flow Field Measurement Results at L-0 Stator Exit. The time-averaged results for operating point OP-1 are presented in this section of the paper. The operating conditions for OP-1 are presented in Table 2. The results are circumferentially area averaged over one stator pitch, and the first measurement point is at 96% of the span, which eliminates the influence of the probe access hole on the mainstream flow. Additionally, the minimum and maximum values obtained with the time-resolved data are plotted on the current graphs with solid lines.

Figures 5(a) and 5(b) show the spanwise distribution of the total and static pressure coefficients for OP-1 according to Eqs. (1) and (2). As shown in Fig. 5(a), the total pressure coefficient is 0.06, up to 80–85% span and increases progressively to 0.07, up to 96% of the blade span. The static pressure coefficient presented in Fig. 5(b) is 0.035, up to 80–85% and remains fairly constant up to 96% of the blade span with a small reduction at 87% span. The peak-to-peak fluctuations are relatively low in the lower region of the top 30% of the blade span and increase up to 3 times in the outer region for both coefficients C_{pt} and C_{ps} , as shown in Figs. 5(a) and 5(b).

Figure 6(a) present the delta yaw angle, and Fig. 6(b) the pitch angle. In Fig. 6(a), the absolute yaw angle measured with the FRAP-HTH probe is subtracted from the mean value of the blade metal angle according to the following equation:

$$\Delta\varphi = \varphi_{ma} - \varphi_{abs,FRAP-HTH} \quad (3)$$

Negative values imply flow underturning, while positive values imply flow overturning. In general, the flow follows the blade

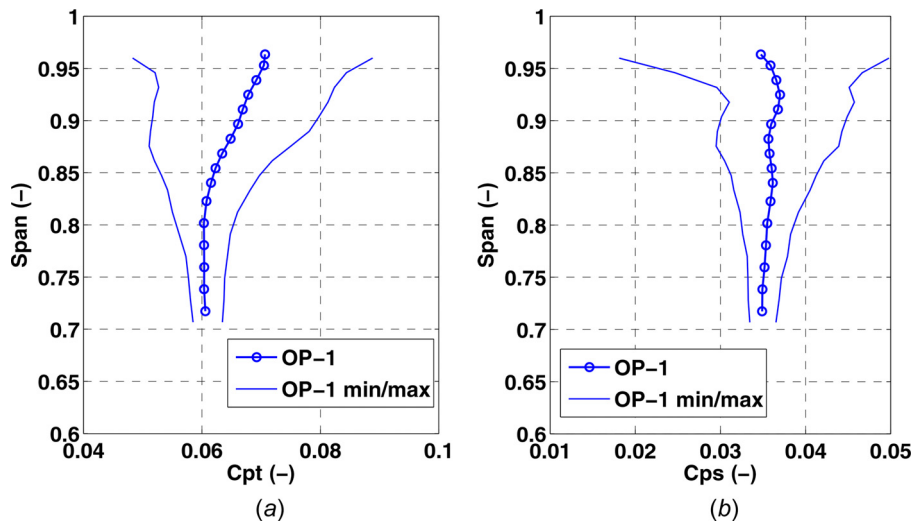


Fig. 5 Circumferentially area-averaged spanwise distribution of C_{pt} (-) (a) and C_{ps} (-) (b) with the minimum and maximum values obtained from the time-resolved data

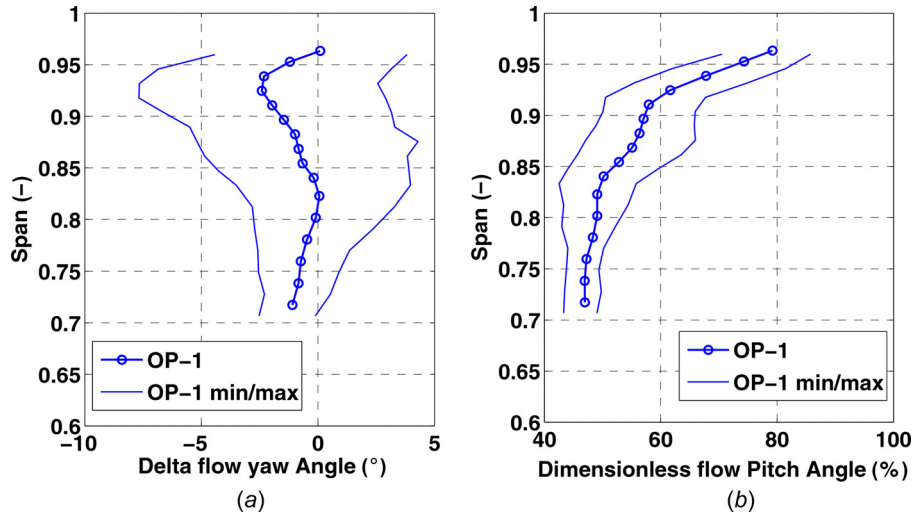


Fig. 6 Circumferentially area-averaged spanwise distribution of delta flow yaw angle (deg) (a) and dimensionless flow pitch angle (-) (b) with the minimum and maximum values obtained from the time-resolved data

metal angle with a small underturning of 2.5 deg on average at 93% span. The flow pitch angle in Fig. 6(b) is the ratio of the measured pitch angle with the FRAP-HTH probe and the flare angle of the turbine (annulus angle at the meridional plane of the steam turbine casing). Values of 100% pitch imply that the flow has the same pitch angle as the flare angle of the steam turbine and a 0% pitch angle indicates that the flow is parallel to the rotating axis of the machine. As depicted in Fig. 6(b), the flow pitch angle is approximately 60% of the flare angle up to 90% span, and it reaches approximately 90% of the flare angle from 90% to 96% of the blade span.

In order to analyze the flow field further, the blade span is divided into two regions: the outer range and the inner range of the top 30% of the blade span where all measurements were conducted. In the outer range region, the flow relative to the rotor blade is supersonic, and in the inner range the flow relative to the rotor blade is subsonic. Table 3 demonstrates the percentage of the peak-to-peak fluctuations over the mean value for the four flow quantities: Cpt, Cps, delta yaw angle, and the dimensionless flow pitch angle as presented in Figs. 5 and 6. In order to calculate these values, the following equation was used:

$$\frac{\text{rms}(\tilde{Fq}_{\max} - \tilde{Fq}_{\min})}{\text{mean}(\tilde{Fq})} \times 100\% \Bigg|_{\text{span region}} \quad (4)$$

In Table 3, all flow quantities are in percentage except the delta yaw angle, where the peak-to-peak difference is used since the

Table 3 Peak to peak fluctuations of the main flow field quantities as a function of the mean value for OP-1 for supersonic and subsonic regions of the span

Flow quantity	Region	OP-1 (%)
Cpt	Supersonic	±20.1
	Subsonic	±5.8
Cps	Supersonic	±22.5
	Subsonic	±6.6
Delta yaw angle	Supersonic	±4.5 deg
	Subsonic	±1.9 deg
Dimensionless pitch angle	Supersonic	±11.9
	Subsonic	±6.1

denominator of Eq. (4) gets values very close to zero. As expected and presented in Table 3, the supersonic region experiences greater peak-to-peak fluctuations in all flow quantities. In particular, the total and static pressure coefficient is about 3.5 times larger in the supersonic region as compared to the subsonic. Regarding the flow angles, the peak-to-peak fluctuations in yaw and pitch angles have been doubled in the supersonic region compared to the subsonic. The variations in the yaw angle are ±4.5 deg, and the variations in flow pitch angle are ±11.9% of the mean value. It is worth noting that the unsteady fluctuations in the subsonic region are in the range of 5–10% of the mean value for each flow quantity, which is a typical range for unsteadiness downstream of a stator.

The relative supersonic speed at the last stage rotor blade results in a bow shock traveling with the rotor leading edge and interacting with the stator exit flow as described by Senoo [3,6]. This bow shock is responsible for the large flow unsteadiness measured in the supersonic region and presented in Table 3, and it induces up to 2 times higher rotor relative inflow angles' variation in comparison to the subsonic region. The time-resolved data presented in the following paragraph would be of use for the study of differences between the subsonic and supersonic regions of the L-0 rotor blade and further analysis of the flow field.

Time-Resolved Flow Field Measurement Results at L-0 Stator Exit

Results at Spanwise Locations of 90% and 75%. In order to further understand the results in Figs. 5 and 6 and be able to compare the sub- and supersonic flow regions, the time-resolved measurements are presented in this section for four rotor blade-passing periods of L-0 rotor. In particular, the time–distance plots are presented at 90% and 75% of the blade span where the flow is supersonic and subsonic, respectively, relative to the rotor inlet. In the time–distance plots, fixed flow features relative to the stationary frame appear as vertical lines (i.e., stator wake), and features traveling with the downstream rotor are visible as inclined parallel structures which are assigned to different rotor blades. The interaction of the downstream rotor influence flow and the stator can be observed in the crossing of those lines. The graphs are plotted for four L-0 rotor blade-passing periods (y-axis), since within this time five full L-1 rotor blade-passing periods have been completed.

The static pressure coefficient for the supersonic (90% span) and subsonic (75% span) spanwise locations is plotted in

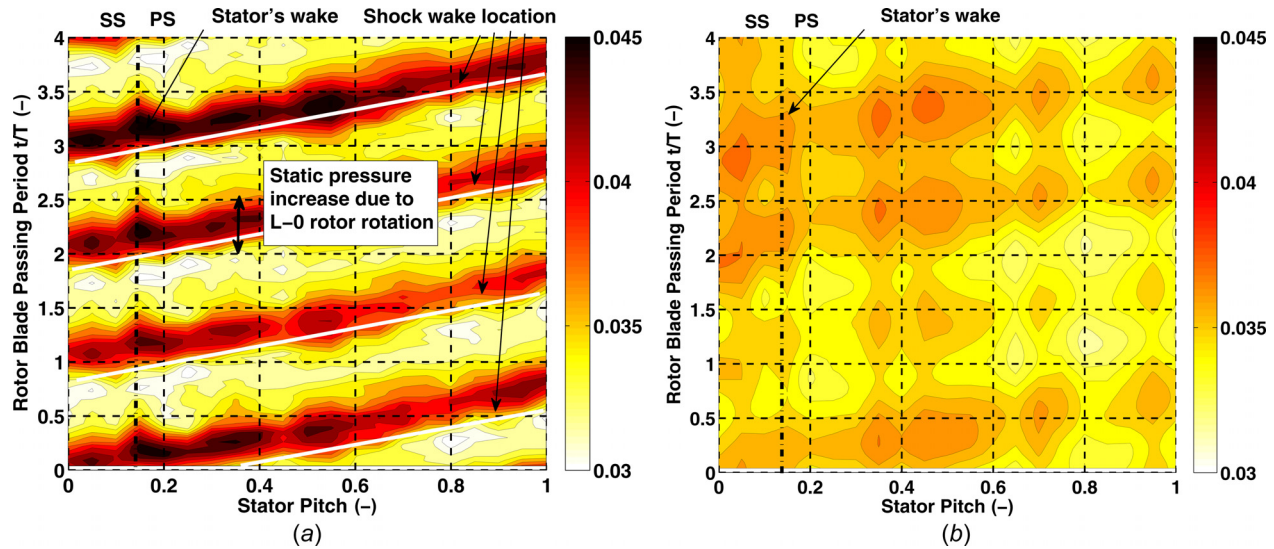


Fig. 7 Circumferential distribution of Cps (-) at L-0 stator exit for OP-1 at 90% (a) and 75% (b) span

Figs. 7(a) and 7(b), respectively. Following the stator's exit flow mean angle, the location of the intersecting wake was found at approximately 0.15 stator pitch. As highlighted in Figs. 7(a) and 7(b), the stator suction and pressure sides are located on the left and right of the stator wakes, respectively. The observer looks upstream in all time–distance plots. As mentioned previously, the spatial resolution is limited to 21 circumferential traverses covering one stator passage. Therefore, it is possible that very small features such as the stator wake are resolved with really limited samples. As presented in Fig. 7(a), the variation in Cps and therefore in static pressure in a fixed stator pitch location is due to the downstream rotor rotation. High values of Cps would indicate the downstream rotor influence flow field and low values of Cps the downstream rotor passage. The flow field in the subsonic region at the L-0 stator exit exhibits lower unsteadiness than presented earlier and shown in Fig. 7(b). In particular, the peak-to-peak fluctuations in the stator's wake region are below 5% of the mean value and remain fairly constant in the entire stator passage. It should be noted that the variation of Cps at different blade-passing periods (i.e., $t/T = 1.75$ compared to 2.25 at 0.4 stator pitch) is most probably related to the complex flow field of the upstream stages. Their signature in this spanwise location with the absence of the downstream bow shock was expected to be more evident than it is.

Figure 8 shows the total and static pressure coefficient as a function of stator pitch at 90% span when the flow is completely frozen at $t/T = 1.5$. The static pressure coefficient curve in Fig. 8 is generated from the results in Fig. 7(a) at the fixed rotor blade-passing period $t/T = 1.5$. As presented in Fig. 8, the circumferential extension of the influence field from the downstream rotor is depicted in the Cps value from 0.3 to 0.9 of the stator pitch. This becomes more obvious in the total pressure coefficient of the same figure as a result of the improved signal to noise ratio on the total pressure. The region of high Cpt values of Fig. 8 is related to the influence of the bow shock from the downstream rotor and the region of the low Cpt values to the downstream rotor passage as explained previously.

The regions of high and low static pressure, as presented in Fig. 7(a), correspond well with flow overturning and underturning, respectively, as indicated in Fig. 9 for the supersonic region at 90% of the blade span. As shown in Fig. 9, the peak-to-peak fluctuations of the yaw angle in the vicinity of the stator wake are ± 5.1 deg indicating the influence of L-0 rotor due to rotation. Nevertheless, the periodical impingement of the rotor attached bow shock on the stator suction side does not seem to result in the separation of the stator's boundary layer. No clear evidences of

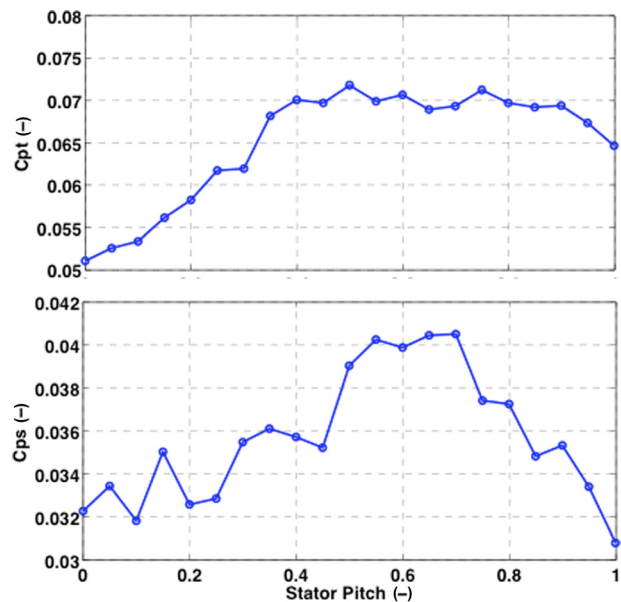


Fig. 8 Total and static pressure coefficients at 90% span for OP-1 at $t/T = 1.5$

stator wake periodical widening could be identified in the static pressure and yaw angle time-resolved results shown in Figs. 7(a) and 9, respectively.

Coarse Droplet Measurement Results at L-0 Stator Exit

Time-Averaged Coarse Droplet Spatial Distribution Analysis. This section presents the time-averaged results of the coarse water droplets distribution downstream of L-0 stator for two operating conditions, OP-2 and OP-3 as presented in Table 2. As mentioned previously, the measurement plane of the droplet measurements is located at approximately $x/s = 0.02$ downstream of the stator and the observer looks upstream. In addition, stator schematics with the approximate location of their trailing edges are plotted in order to provide a better view of the stator passage to the reader. Although the measurements were conducted at the last 30% of the blade span for one stator pitch, the results presented in the current paragraph are focused at the blade span between 68% and 82%, since this region has a substantial droplet count within the

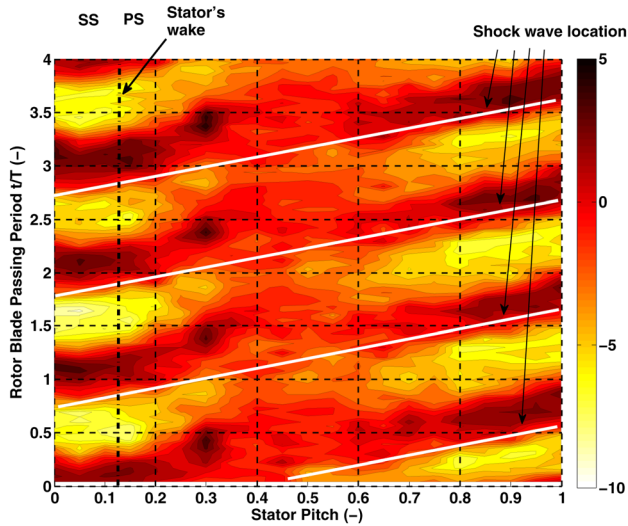


Fig. 9 Circumferential distribution of delta yaw angle (deg) at L-0 stator exit for OP-1 at 90% span

operating range of the FRAP-OB probe. Results from operating point OP-3 cover 1.2 of the stator pitch in order to further support the discussion of the droplet spatial distribution analysis. It has to be mentioned that all results comprise droplet sizes above the minimum probe's detection limit of $D_d > 30 \mu\text{m}$.

Figure 10 shows the time-averaged contour plots of the droplet rate for the two operating points, OP-2 and OP-3. The droplet rate is the number of coarse water droplets recorded for each point of the measurement grid for one rotor revolution. As presented in Figs. 10(a) and 10(b), all droplets above $30 \mu\text{m}$ in diameter cover the entire stator passage for both operating points of the steam turbine. At specific locations in the stator wake region, droplets were not detected. These locations are indicated in Fig. 10(a) at 0.3 pitch and at 70% span and in Fig. 10(b) at 0 pitch and at 70–75% span.

The results of the Sauter mean diameter for OP-3 and OP-2 are plotted in Figs. 11(a) and 11(b), respectively. As shown in the two figures, the largest droplets were detected in the vicinity of the stator suction side, and the smallest droplets were measured closer to the pressure side of the last stage stator.

In order to further understand the droplet formation mechanism for the given operating conditions, the time-averaged droplet mass rate was calculated according to the equation given as follows:

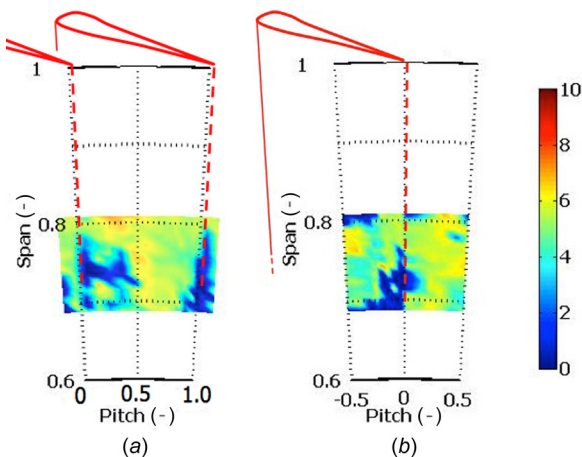


Fig. 10 Time-averaged results of droplet rate (#droplet/rev) for (a) OP-3 and (b) OP-2 at L-0 stator exit

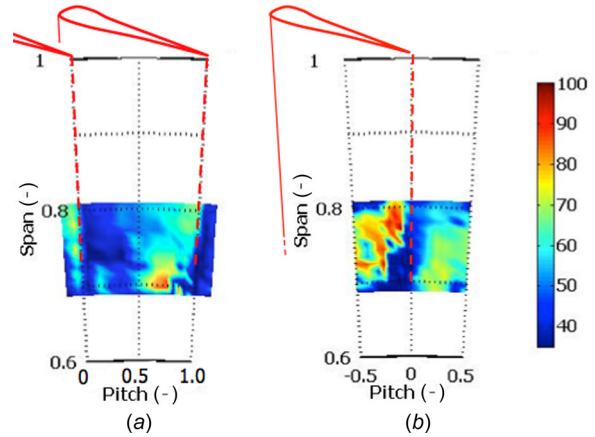


Fig. 11 Time-averaged results of Sauter mean droplet diameter (μm) for (a) OP-3 and (b) OP-2 at L-0 stator exit

$$M_d = N_i \frac{4}{3} \pi r_{d10,i}^3 \rho_d \quad (5)$$

The droplet mass rate is calculated by multiplying the number of droplets measured at each measurement grid location with their volume and density. The droplet volume is calculated using the measurements of the droplet diameter obtained with the FRAP-OB probe. Thus, the droplet mass rate is a measure of the water content and as a consequence should be proportional to the wetness mass fraction.

The results from the droplet mass rate for the operating points OP-3 and OP-2 are presented in Figs. 12(a) and 12(b), respectively. The figures show that the droplet mass rate increases at the vicinity of the stator's suction side in both operating conditions. Moore and Sieverding [24] describe this mechanism with the formation of a film on the suction side of the stator from water droplets that are centrifuged from the second to last row of the moving blades. Further evidence of this particular distribution is found in Fig. 12(a), since the results cover 1.2 of the stator pitch for this particular operating point. At OP-3 (Fig. 12(a)), there is a high rate of water content between 0.5 and 1 of the stator pitch for the measured spanwise range. The results for OP-2 (Fig. 12(b)) also demonstrate high levels of water content in the vicinity of the stator's suction side between -0.5 and 0 of the stator pitch and in particular in the spanwise region between 70% and 82%. The values have increased by 50% from the operating point OP-3 to OP-2 as shown in Figs. 12(a) and 12(b), respectively.

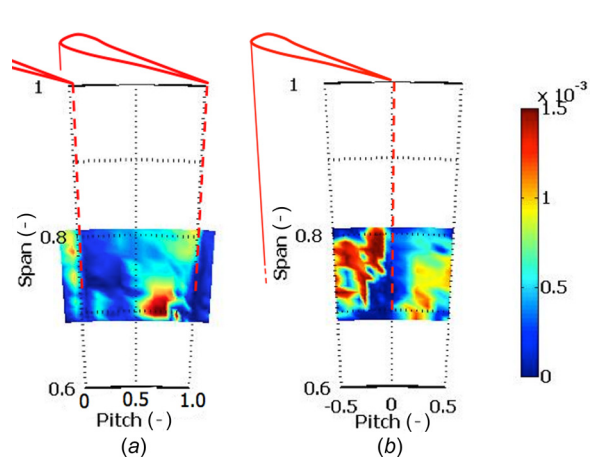


Fig. 12 Time-averaged results of droplet mass rate (mg/rev) for (a) OP-3 and (b) OP-2 at L-0 stator exit

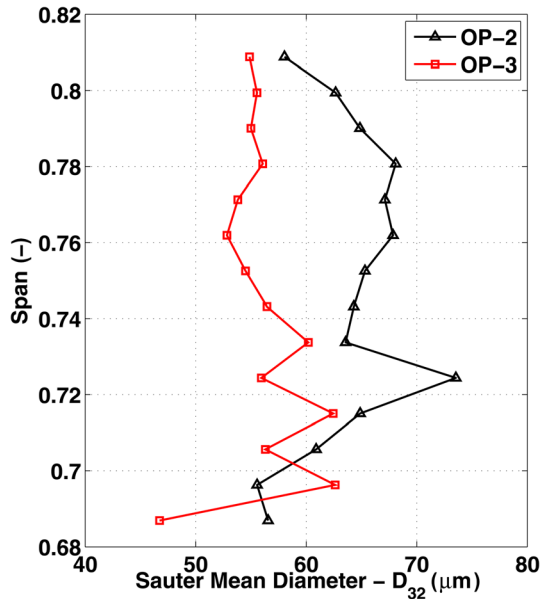


Fig. 13 Sauter mean droplet diameter for OP-2 ($T_{in} = 270^\circ\text{C}$) and OP-3 ($T_{in} = 220^\circ\text{C}$) at L-0 stator exit

On average, the wetness mass fraction in OP-3 is greater than in OP-2, since the turbine inlet temperature is reduced. However, as stated by Crane [5], the contribution of coarse water droplets to the total wetness fraction is only 5–10% of the overall droplet mass. This implies that the fog droplets primarily determine the wetness fraction at a specific operating condition. In addition, Moore and Sieverding [24] indicate that when temperature is reduced, the droplets' size reduces and the concentration increases. Based on these two facts, it is believed that the reduced droplet mass rate in OP-3 compared to OP-2 is most probably due to a shift in the total droplet distribution (fog and coarse) toward smaller sizes. The final size of the droplet diameter cannot be

depicted in the current results, since the FRAP-OB only measures droplets with a diameter greater than $D_d > 30\ \mu\text{m}$. However, this trend is also shown on the Sauter mean diameter as it is indicated in Fig. 13, with a change from $65\ \mu\text{m}$ to $55\ \mu\text{m}$ when the operating point of the steam turbine changes from OP-2 to OP-3.

According to Eq. (5), the elevated values of water content at the vicinity of the stator's suction side imply that coarse water droplets are located in that region (see Fig. 11), since coarse droplets were found almost uniformly in the entire stator pitch, as indicated in Fig. 10. This is also depicted in Fig. 14 with the distributions of the droplet diameter for a fixed spanwise location at 75% span for OP-2.

The Sauter mean diameter decreases progressively starting at $80.2\ \mu\text{m}$ at the vicinity of the stator suction side (pitch = -0.25) until it reaches its minimum value in the vicinity of the stator's pressure side (pitch = $+0.25$) with $D_{32} = 37.3\ \mu\text{m}$. This is the first time according to the authors' knowledge that droplet plane measurements have been conducted at the stator exit of the last stage for the entire stator pitch. The current results are trying to supplement the existing theory [5,17,25,26] which states that large droplets are generated from the development of a liquid thin film on the stationary blades, due to the deposition of submicron droplets formed by nucleation in the main steam flow, and later sheds from the trailing edge of the stator. It is believed that the presence of suction slits at the pressure side of the stator reduce the size of the coarse droplets, which is beneficial for the erosion process. As a result, the droplet coagulation mechanism described by Moore and Sieverding [24] where fog and coarse droplets are mixed in the freestream could potentially result in the droplet spatial distribution which was measured in the current work and presented in this section of this paper in Figs. 12(a) and 12(b).

Time-Resolved Coarse Droplet Measurements. Further evidence of the droplet locations is presented with the time-resolved results obtained with the FRAP-OB probe. Figure 15 shows the circumferential distribution at 78% of the stator span of the time-resolved droplet mass rate as it was measured with the FRAP-OB probe for operating OP-2 where flow field data are also available. In order to calculate this quantity, four rotor blade passages are partitioned into 15 sections with a time interval of $t_{int} = 4/ (15 \times \text{BPF})$, and the individual droplets that were found in each of

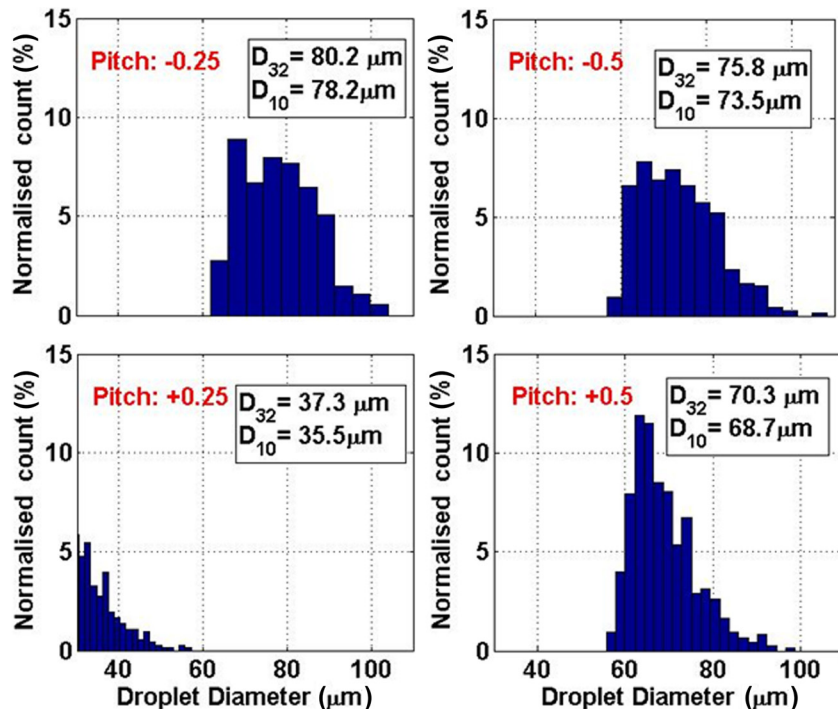


Fig. 14 Droplet diameter distribution for OP-2 at 75% for four different circumferential locations at pitch: -0.25 , -0.5 , $+0.5$, and $+0.25$ (see Fig. 12(b))

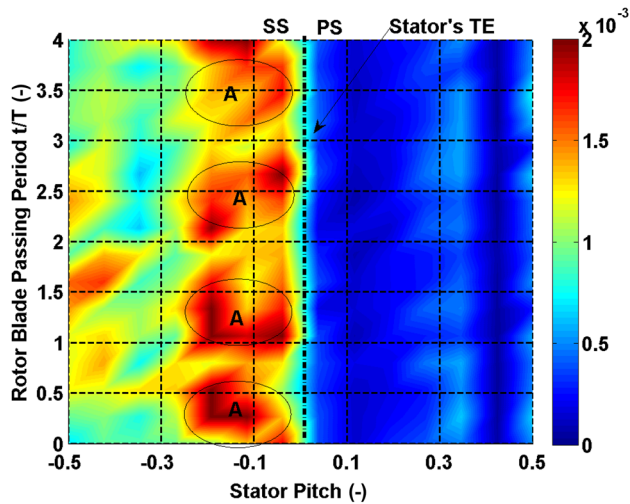


Fig. 15 Circumferential distribution of measured droplet mass rate (mg/s) at L-0 stator exit for OP-2 at 78% span

these sections were phase-locked over 88 rotor revolutions. As presented in Fig. 15, the time-resolved droplet mass rate is modulated by the rotor blade-passing period. This is highlighted with the feature A located at -0.15 of the stator pitch which is repeated at $t/T = 0.25, 1.25, 2.25,$ and 3.25 . As presented in Fig. 12(b), the water content from in the stator pitch from 0 to 0.5 has been reduced by 60% on average. As a consequence, the unsteady fluctuations shown in Fig. 15 are also reduced from 0 to 0.5 stator pitch and are only present at 0.4 of the stator pitch and still modulated with the rotor blade-passing period.

In order to further analyze the droplet spatial distribution, the time-resolved static pressure coefficient is plotted for the same operating point and spanwise location in Fig. 16(a). The L-0 stator wake intersection for two consecutive stator blades is found at 0 and 1 stator pitch for this operating condition. The feature A with high water content at -0.15 stator pitch as indicated in Fig. 15 corresponds to region A with low local static pressure at 0.85 stator pitch, as shown in Fig. 17. The location of -0.15 (0, trailing edge $-0.15 = 0.15$) pitch of Fig. 15 corresponds to 0.85 (1, trailing $-0.15 = 0.85$) in Fig. 16(a) as the two measurement planes are not the same axial downstream distance from the stator trailing edge as each other. The unsteady interaction of the downstream rotor blades with the stator wake and freestream results in pressure fluctuations which could potentially influence the condensation process [27] and might effect the coarse droplet coagulation mixing mechanism. As a consequence, it is believed that the regions where coarse droplets were measured could be a result of a

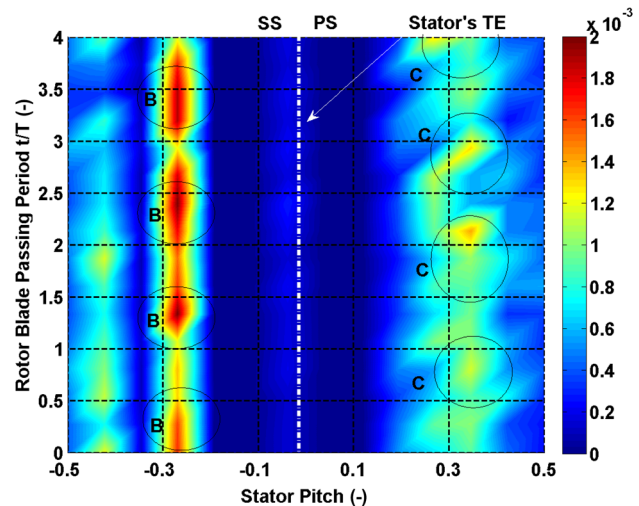


Fig. 17 Circumferential distribution of measured droplet mass rate (mg/s) at L-0 stator exit for OP-2 at 71% span

mixing process mainly due to coagulation and will depend on the stator rotor interactions, as presented in Figs. 15 and 16(a). The novel measures with the FRAP-OB probe revealed a spatial distribution for the coarse droplets for two different operating points that are also modulated with the downstream rotor blade-passing period. Since the droplet formation mechanism is strongly dependent on the operating point of the machine as well as on the stator geometry (suction slits, trailing shape, etc.), it has to be further investigated and cross-compared with measurements at different LP steam turbine stator blades and various operating conditions.

It is worth noting the correlation of high streamwise vorticity with regions of high water content measured with the FRAP-OB probe. This is depicted in Fig. 16(b) with the dimensionless streamwise vorticity at 78% span for OP-2. As presented in Fig. 15, the locations of high water content (features A, Fig. 15) coincide with regions of high alternating streamwise vorticity in Fig. 16(b). One could associate the regions of high vorticity with regions of high mixing in the flow field and suggest that this pattern occurs as a consequence of fog and coarse water droplet coagulation as described earlier. In the same graph, there is a location at 0.4 stator pitch with even greater values of streamwise vorticity which are most probably associated to the complex flow field generated from the upstream four stages.

Similar results and trends for the spanwise location at 71% are presented in Figs. 17 and 18(a). Figure 17 shows the coarse droplet mass rate for operating point OP-2 for four consecutive rotor

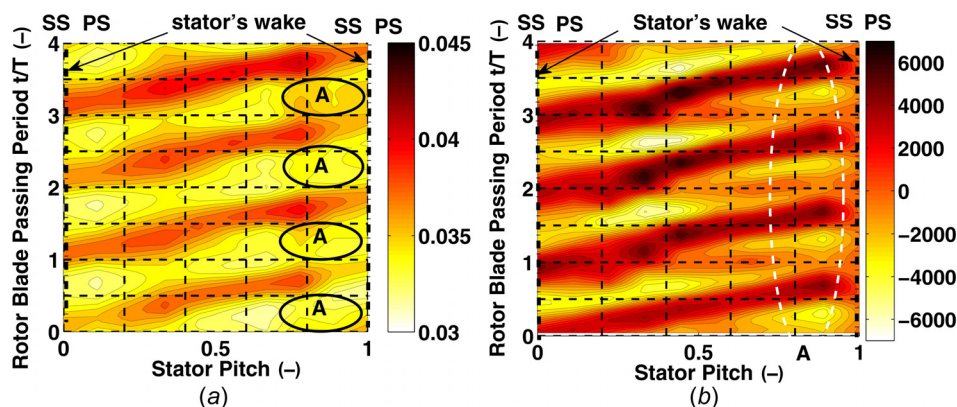


Fig. 16 Circumferential distribution of Cps (-) (a) and nondimensional streamwise vorticity (-) (b) at L-0 stator exit for OP-2 at 78% span

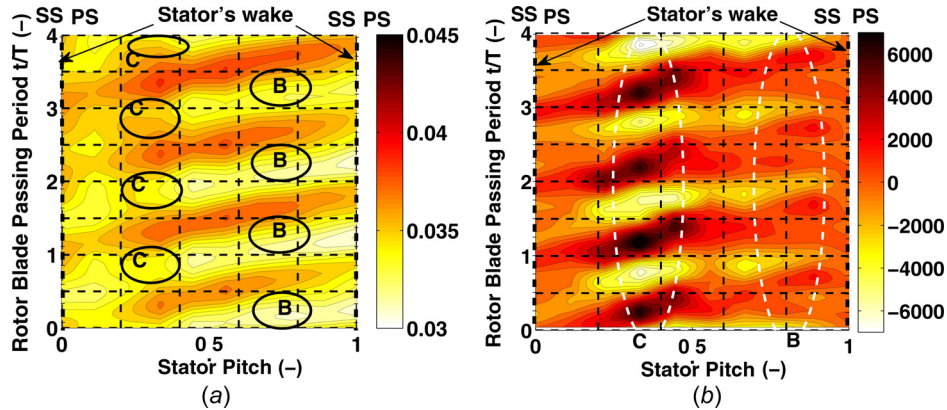


Fig. 18 Circumferential distribution of C_{ps} (-) (a) and nondimensional streamwise vorticity (-) (b) at L-0 stator exit for OP-2 at 71% span

blade-passing periods. The features B and C located at -0.25 and $+0.35$ stator pitch, respectively, are modulated with the rotor blade-passing period. The results at 71% span show the same behavior as the previous spanwise location. The features with high water content B as indicated in Fig. 17 correspond to regions B with low local static pressure at 0.75 stator pitch as indicated in Fig. 18(a). On the other hand, the features highlighted as C in Fig. 17 correspond to regions with low static pressure coefficient C at 0.35 stator pitch in Fig. 18(a).

The streamwise vorticity for this spanwise location is shown in Fig. 17. As presented in Fig. 17, the locations of high water content (features B and C, Fig. 17) coincide with regions of high alternating streamwise vorticity in Fig. 18(b). Again, the regions of high vorticity could be associated to regions of high mixing in the flow field, as a consequence of fog and coarse water droplet coagulation. Further investigation on the topic is needed in order to better understand the droplets' formation mechanisms in the last stage of an LP steam turbine.

Conclusions

- This paper presents combined time-resolved coarse droplet and flow field measurements over a stator pitch conducted at the nozzle exit of the last stage of a low-pressure steam turbine with supersonic flow conditions near the blade tip.
- Results have shown that the attached bow shock at the rotor leading edge increases the flow unsteadiness compared to the subsonic region. It induces rotor relative inflow angles up to 2 times higher than in the subsonic region.
- The static pressure unsteadiness for the supersonic and subsonic regions is $\pm 22.5\%$ and $\pm 6.6\%$ of the mean value, respectively. The yaw angle unsteadiness for the supersonic and subsonic regions is ± 4.5 deg and ± 1.9 deg of the mean value, respectively.
- The periodical impingement of the rotor attached bow shock on the upstream stator suction side does not seem to result in the separation of the stator's boundary layer as no clear evidences of stator wake periodical widening could be identified in the static pressure and yaw angle time-resolved results.
- The coarse water droplets' range was measured from 37 to 80 μm in Sauter mean diameter, and they were found to be between 68% and 82% span over the entire stator pitch. The largest droplets were measured at the vicinity of the stator suction side. The low inlet temperature seems to exhibit droplets with a lower Sauter mean diameter; however, further investigations are needed to understand the underlying coarse water droplet formation mechanism.
- The suction slit seems to perform well in reducing the amount of coarse droplets present in the pressure side of the stator wake.

- Unsteady coarse droplet measurements at the stator exit of the last stage showed that the droplet mass rate is modulated by the downstream rotor blade-passing period.

Acknowledgment

The authors would like to thank Mitsubishi Hitachi Power Systems for the financial and technical support provided over the course of the current project. Special thanks go for Mr. C. Duan and Mr. K. Ishibashi from MHPS for their active support during the measurement campaigns in Japan as well as their support in providing essential information to complete the data analysis. Finally, the authors would like to acknowledge the entire MHPS research team at Hitachi city in Japan for making these measurements possible.

Nomenclature

C_{ps}	= static pressure coefficient
C_{pt}	= total pressure coefficient
D	= diameter (m)
M	= droplet mass rate ($\mu\text{g}/\text{rev}$)
N	= droplet rate (#droplets/rev)
P, p	= pressure (Pa)
r	= radius (μm)
s	= axial gap between L-0 stator rotor (mm)
t	= time instant
T	= temperature, time period ($^{\circ}\text{C}$)
x	= axial distance downstream stator (mm)
ρ	= density (kg/m^3)

Greek Symbols

γ	= flow pitch angle (deg)
φ	= flow yaw angle (deg)

Subscripts

abs	= absolute
d	= droplet
i	= measurement point at specific grid location
s	= static
t	= total
10	= arithmetic mean droplet diameter
32	= Sauter mean droplet diameter

Superscripts

\sim	= time-resolved data (phase-locked)
$-$	= time-averaged data (mean value)

Abbreviations

- BPF = blade-passing frequency
Fq = flow field quantity (yaw, pitch angle, etc.)
FRAP-HTH = high-temperature, fast response aerodynamic heated probe
FRAP-OB = fast response optical backscatter probe
ma = mean value of L-0 stator metal angle
MHPS = Mitsubishi Hitachi Power Systems
OP = operating point
PS = pressure side
rms = root mean square
SS = suction side
TE = L-0 stator's trailing edge

References

- [1] Haraguchi, M., Nakamura, T., Yoda, H., Kudo, T., and Senoo, S., 2013, "Nuclear Steam Turbine With 60 Inch Last Stage Blade," *ASME Paper No. ICONE21-16600*.
- [2] Shibukawa, N., Iwasaki, Y., Takada, Y., Murakami, I., Suzuki, T., and Fukushima, T., 2014, "An Experimental Investigation of the Influence of Flash-Back Flow on Last Three Stages of Low Pressure Steam Turbines," *ASME Paper No. GT2014-26897*.
- [3] Senoo, S., 2012, "Development of Design Method for Supersonic Turbine Aerofoils Near the Tip of Long Blades in Steam Turbines: Part 1—Overall Configuration," *ASME Paper No. GT2012-68218*.
- [4] Havakechian, S., and Denton, J., 2015, "Three-Dimensional Blade-Stacking Strategies and Understanding of Flow Physics in Low-Pressure Steam Turbines—Part I: Three-Dimensional Stacking Mechanisms," *ASME J. Eng. Gas Turbines Power*, **138**(5), p. 052603.
- [5] Crane, R. I., 2004, "Droplet Deposition in Steam Turbines," *Proc. Inst. Mech. Eng., Part C*, **218**(8), pp. 859–870.
- [6] Senoo, S., and Ono, H., 2013, "Development of Design Method for Supersonic Turbine Aerofoils Near the Tip of Long Blades in Steam Turbines: Part 2—Configuration Details and Validation," *ASME Paper No. GT2013-94039*.
- [7] Gerschütz, W., Casey, M., and Truckenmüller, F., 2005, "Experimental Investigations of Rotating Flow Instabilities in the Last Stage of a Low-Pressure Model Steam Turbine During Windage," *Proc. Inst. Mech. Eng., Part A*, **219**(6), pp. 499–510.
- [8] Segawa, K., Senoo, S., Kudo, T., Nakamura, T., and Shibashita, N., 2012, "Steady and Unsteady Flow Measurements Under Low Load Conditions in a Low Pressure Model Steam Turbine," *ASME Paper No. ICONE20-POWER2012-54862*.
- [9] Miyake, S., Koda, I., Yamamoto, S., Sasao, Y., Momma, K., Miyawaki, T., and Ooyama, H., 2014, "Unsteady Wake and Vortex Interactions in 3-D Steam Turbine Low Pressure Final Three Stages," *ASME Paper No. GT2014-25491*.
- [10] Kleitz, A., and Dorey, J. M., 2004, "Instrumentation for Wet Steam," *Proc. Inst. Mech. Eng., Part C*, **218**(8), pp. 811–842.
- [11] Walters, P., and Skingley, P., 1979, "An Optical Instrument for Measuring the Wetness Fraction and Droplet Size of Wet Steam Flows in LP Turbines," *Proc. Inst. Mech. Eng., Part C*, **141**(79), pp. 337–348.
- [12] Walters, P. T., 1987, "Wetness and Efficiency Measurements in L.P. Turbines With an Optical Probe as an Aid to Improving Performance," *ASME J. Eng. Gas Turbines Power*, **109**(1), pp. 85–91.
- [13] Tatsuno, K., and Nagao, S., 1986, "Water Droplet Size Measurements in an Experimental Steam Turbine Using an Optical Fiber Droplet Sizer," *ASME J. Heat Transfer*, **108**(4), pp. 939–945.
- [14] Cai, X., Ning, T., Niu, F., Wu, G., and Song, Y., 2009, "Investigation of Wet Steam Flow in a 300 MW Direct Air-Cooling Steam Turbine. Part 1: Measurement Principles, Probe, and Wetness," *Proc. Inst. Mech. Eng., Part A*, **223**(5), pp. 625–634.
- [15] Young, J. B., and Yeoh, C. C., 1984, "The Effect of Droplet Size on the Flow in the Last Stage of a One-Third Scale Model Low-Pressure Turbine," *Proc. Inst. Mech. Eng., Part A*, **198**(13), pp. 309–316.
- [16] Schatz, M., and Casey, M., 2007, "Design and Testing of a New Miniature Combined Optical/Pneumatic Wedge Probe for the Measurement of Steam Wetness," *AIP Conf. Proc.*, **914**(1), pp. 464–479.
- [17] Cai, X., Ning, D., Yu, J., Li, J., Ma, L., Tian, C., and Gao, W., 2014, "Coarse Water in Low-Pressure Steam Turbines," *Proc. Inst. Mech. Eng., Part A*, **228**(2), pp. 153–167.
- [18] Fan, X., Jia, Z., Zhang, J., and Cai, X., 2009, "A Video Probe Measurement System for Coarse Water Droplets in LP Steam Turbine," *J. Phys.: Conf. Ser.*, **147**(1), p. 012065.
- [19] Bosdas, I., Mansour, M., Kalfas, A. I., Abhari, R. S., and Senoo, S., 2015, "Unsteady Wet Steam Flow Field Measurements in the Last Stage of Low Pressure Steam Turbine," *ASME J. Eng. Gas Turbines Power*, **138**(3), p. 032601.
- [20] Bosdas, I., Mansour, M., Kalfas, A. I., and Abhari, R. S., 2016, "An Optical Backscatter Probe for Time Resolved Droplet Measurements in Turbomachines," *Meas. Sci. Technol.*, **27**(1), p. 015204.
- [21] Duan, C., Ishibashi, K., Senoo, S., Bosdas, I., Mansour, M., Kalfas, A. I., and Abhari, R. S., 2016, "Unsteady Wet Steam Flow Measurements in a Low-Pressure Test Steam Turbine," *Int. J. Fluid Mach. Sys.*, **9**(1), pp. 85–94.
- [22] Bosdas, I., Mansour, M., Kalfas, A. I., and Abhari, R. S., 2016, "A Fast Response Miniature Probe for Wet Steam Flow Field Measurements," *Meas. Sci. Technol.*, **27**(12), p. 125901.
- [23] Rollinger, B., Morris, O., and Abhari, R. S., 2011, "Stable Tin Droplets for LPP EUV Sources," *Proc. SPIE*, **7969**, p. 79692W.
- [24] Moore, M. J., and Sieverding, C. H., 1976, *Two-Phase Steam Flow in Turbines and Separators: Theory—Instrumentation—Engineering*, Hemisphere, Washington, DC.
- [25] Christie, D. G., Hayward, G. W., Lowe, H. J., MacDonald, A. N., and Sculpher, P., 1965, "The Formation of Water Drops Which Cause Turbine Blade Erosion," *Proc. Inst. Mech. Eng.*, **180**(15), pp. 13–22.
- [26] Li, C., Wang, X., Cheng, D., and Sun, B., 2008, "Experimental Study on Effects of Slot Hot Blowing on Secondary Water Droplet Size and Water Film Thickness," *ASME J. Eng. Gas Turbines Power*, **131**(3), p. 033001.
- [27] Starzmann, J., Schatz, M., Casey, M. V., Mayer, J. F., and Sieverding, F., 2011, "Modelling and Validation of Wet Steam Flow in a Low Pressure Steam Turbine," *ASME Paper No. GT2011-45672*.